ROYAL SOCIETY
OPEN SCIENCE

royalsocietypublishing.org/journal/rsos

Research

Cite this article: Izawa T, James LA, Yethiraj A. 2026 The decay of saline surfactant foams: a study at macroscopic and bubble scales. *R. Soc. Open Sci.* **13**: 251765.
https://doi.org/10.1098/rsos.251765

Received: 14 September 2025
Accepted: 26 December 2025

Subject Category:
Physics and biophysics

Subject Areas:
physical chemistry, materials science, chemical engineering, soft matter

Keywords:
foam, salinity, persistence, decay, stability

Author for correspondence:
Anand Yethiraj
e-mails: ayethira@uoguelph.ca; ayethiraj@mun.ca

Supplementary material is available online at https://doi.org/10.6084/m9.figshare.c.8304092.

The decay of saline surfactant foams: a study at macroscopic and bubble scales

Tatsuo Izawa[1,2], Lesley Anne James[2] and Anand Yethiraj[1,3]

[1] Department of Physics and Physical Oceanography, Soft Matter Lab, and [2] Faculty of Engineering and Applied Science, Memorial University of Newfoundland, St John's, Newfoundland and Labrador, Canada
[3] Department of Physics, University of Guelph, Guelph, Ontario, Canada

AY, 0000-0003-1293-2801

How stable are saline, surfactant foams? While the effect of surfactants on stabilizing bubbles in foam is well understood, the effect of salt is not. Saline foams are potentially very important in industrial applications, including enhancing oil recovery, yet there is only a limited understanding of their long-term stability. We report an experimental methodology to simultaneously study the time evolution of foam, at varying salinity, at both macroscopic and bubble scales. With our dual-scale measurements, we track the dynamics of foams made with air and aqueous solutions containing non-ionic surfactant and salts over long times. In macroscopic foam height measurements, we observe that at long times, the foam height decreases logarithmically *for all salinities*, with the height reduction rate being significantly lower at the highest salinity, i.e. the most saline foam persists the longest. Bubble-scale measurements of bubble size, carried out near the bottom of the foam are far more sensitive, providing early warning of the fate of the foam.

1. Introduction

In this work, we study the decay of saline surfactant foams, simultaneously on macroscopic and bubble scales. Surfactant foams have been studied extensively [1–5], but two themes have been less explored: the role of salinity and the correlation of macroscopic foam phenomena with dynamics on the bubble scale.

Liquid foams are useful in a wide range of pharmaceutical, cosmetic [6], therapeutic [7] and other industrial applications [8]. Saline foams, in particular, have industrial relevance. For example, the most accessible injection fluid in the process of enhanced oil recovery [9–11] is saline water (brine), either directly from the ocean or from the reservoir well itself. Injecting brine into an oil

THE ROYAL SOCIETY
PUBLISHING

well can result in viscous fingering when attempting to displace a more-viscous fluid (oil) with a less-viscous fluid (brine). Avoiding this instability is, therefore, crucial because it can create islands of unrecoverable oil. Aqueous foam, composed of air and brine, is a promising visco-elastic (or visco-plastic, given that it flows beyond a threshold yield stress [12]) material because its mechanical response is significantly different from that of either of its gas or liquid constituents [13]. Several studies have investigated fingering instabilities in radial Hele-Shaw cells by changing the viscosity ratio of the displacing and displaced fluids [14] or by controlling the injection flow rate of displacing fluids (Newtonian [15,16] or non-Newtonian [17]) to explore possible strategies to combat the issues arising from the fingering instabilities for industrial applications. Making non-Newtonian saline foams as an injection fluid is thus a viable strategy, but these foams need to persist for very long times.

In the absence of surfactant (apart from possible bio-surfactants in quantities of a few grams per kilogram), salt enhances foaming capacity, as evidenced by the froth in breaking waves in the sea [18,19]. This is surprising from the point of view of the classical Derjaguin–Landau–Verwey–Overbeek (DLVO) theory [20] because one would expect at higher salinity that a stronger Debye–Hückel screening would reduce electrostatic repulsion across liquid films and destabilize them [21]. Since the empirical observations made by Craig *et al.* on the inhibition of bubble coalescence in some salts [18], it is recognized that the behaviour at high salinity relates to ion-specific effects [22]. In the absence of surfactant, there appears to exist a threshold salt concentration above which the bubble coalescence process slows down [23].

The use of a surfactant can significantly affect foamability and foam stability in saline water. Saline foams made with an ionic surfactant (e.g. anionic sodium dodecylsulfate (SDS) [24] or cationic dodecyltrimethylammonium bromide [25]) generally showed higher foamability than saline foams made with a non-ionic surfactant [24,25]. The latter are generally less susceptible to changes in salt concentration, whereas the decay of SDS-containing saline foams appears to be highly dependent on salt concentration [24]. For example, the mean bubble diameter of a non-ionic surfactant foam, when tested with electrolytes or seawater, has been reported to be less sensitive to salinity beyond a characteristic salt concentration [26,27]. Characterizing the time-dependent ageing process of various types of surfactant foams and at different salinity levels is important for making a strategic choice of surfactants.

Foams are known to age through three interdependent processes: foam drainage, which is flow of liquid through the foam films due to gravity, coalescence, where the liquid film between two or more bubbles ruptures, and coarsening, which is caused by gas diffusion between neighbouring bubbles at different pressures [13]. As will be seen below, drainage occurs over relatively short times, while coalescence and coarsening coexist in time. At the macroscopic (bulk, centimetre) scale, foam evolution is quantified in terms of the height (and therefore the volume) of the foam, and simultaneously, the height (or volume) of the liquid level beneath the foam [4]. At the bubble scale, gas exchange through the liquid films occurs between adjacent air bubbles in the foam, leading to slow coarsening. This coarsening is often found to obey the von Neumann law, which was originally applied to domain coarsening in a purely two-dimensional (2D) dry foam [28]: the growth rate of the bubble area (in 2D) is a constant that depends only on the number of bubble neighbours [29,30]. Physics at the bubble scale causes the behaviours observed at the macroscopic scale: it is thus valuable to probe both these length scales.

Studying the time evolution of aqueous foams on the bubble scale in confined geometries often provides more robust characterization in 2D using optical imaging techniques [5,11,31]. For practical applications, however, it is essential to probe foam evolution on multiple length scales and for three-dimensional (3D) foams. Osei-Bonsu *et al.* [11] have carried out interesting foam stability experiments at macroscopic and bubble scales, albeit in separate experiments. In this work, we characterize, optically, the evolution of saline non-ionic surfactant foams at both the macroscopic (centimetre) and the bubble (sub-millimetre to millimetre) scales simultaneously in the same sample container. To this end, we first develop an imaging system that can probe the macroscopic-scale and the bubble-scale dynamics of a 3D foam at a container surface. We then examine the salinity dependence of foam dynamics, from short times (dominated by foam drainage) to very long times (dominated by coarsening via gas flux through liquid films and coalescence through film rupture), on both macroscopic and bubble scales.

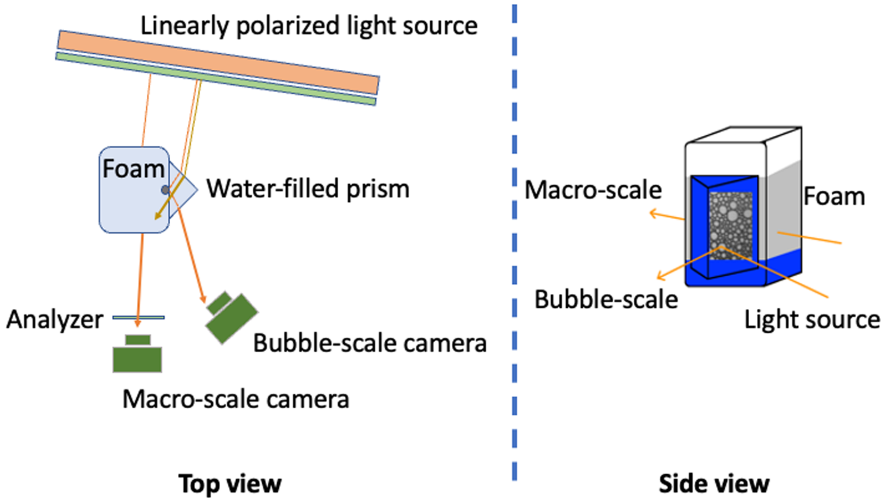

Figure 1. Schematic diagram of the simultaneous dual-scale imaging set-up. Top view (left) and side view (right) for macroscopic ('macro-scale') and bubble-scale imaging. The polarized light from the LCD monitor illuminated the foam sample for both macro-scale and bubble-scale imaging. A polarizer (used as an analyser, crossed with the monitor polarizer) was placed in front of the macro-scale imaging camera.

2. Experimental

2.1. Imaging apparatus

A dual-scale imaging apparatus, shown in figure 1, was constructed to measure the time evolution of the macroscopic foam height while at the same time measuring bubble cross-sectional areas near the bottom of a 3D foam. The measurement timescales ranged from seconds to days. For the macroscopic-scale measurement, a camcorder (JVC GC-PX100) was used to image the entire foam at 1 frame min^{-1} at a spatial resolution of 1280 × 720 pixels. Simultaneously for the bubble-scale measurement, a digital CCD monochrome camera (Qimaging Fast 1394) was used to image at 0.5 frames s^{-1} at a spatial resolution of 1392 × 1040 pixels. As will be expanded on later, this dual-scale set-up was crucial to the results of this work.

To produce a foam, we used a simple bottle shaking technique, a similar foam generation technique used in the Bartsch shaking test [32], at four oscillations of the bottle, back and forth over 100 cm, in 1 s, repeated 10 times [33]. We selected a 16 oz French square bottle (6.5 cm × 6.5 cm × 17 cm) with a screw closure type rubber cap with a wide bottle opening, available at Thermo Fisher Scientific, as a container. The bottom 14 cm of the bottle has uniform cross-section. We carefully attached a hand-made triangular glass prism (refractive index $n=1.51$) filled with water ($n=1.33$) to the bottle using a UV optical glue (Norland Optical Adhesive 63, $n=1.56$) without introducing any air bubbles. The bottle was washed very carefully to minimize any possible contamination by following glass-cleaning suggestions provided by Sigma-Aldrich [34].

An LCD monitor (at 70% brightness with equal RGB setting) was used as an illumination source for both the macroscopic-scale and the bubble-scale imaging. For the macroscopic-scale imaging, we configured the imaging set-up in a transmission geometry that captured the dynamics of bulk foam through a set of crossed polarizers, which reduced background noise and facilitated macroscopic foam height analysis. The monitor provided linearly polarized illumination while a linear polarizer in front of the camera served as the analyser. The distances between the LCD monitor and the foam sample, and between the foam sample and the macro-scale imaging camera, were both approximately 20 cm.

For bubble-scale imaging, we configured the set-up in a total-internal-reflection (TIR) geometry that captured light from the same LCD monitor from a side that was slightly tilted through the water-filled triangular glass prism, while making macroscopic-scale imaging possible. We obtained the surface features of the foam that were close to the interior surface of the bottle through TIR, while rejecting interference from interior bubbles. Electronic supplementary material, figure S1, shows the difference between foam bubbles imaged in transmission (left) and TIR (right) geometries. It was shown in previous work that bubble diameters obtained near the surface of a container scale linearly with the transport mean free path of light in a 3D multiple scattering experiment [35,36]: thus, the TIR method is a good reporter of

Table 1. Composition of synthetic ocean brine for five salinities. As categorized by the US Geological Survey [46], a salinity level less than 1000 parts per million (ppm) is considered as fresh water, 3000–10 000 ppm is moderately saline, and 10 000–35 000 ppm is highly saline (the latter is termed ocean brine). The reservoir brine concentration of 107.133 g kg^{-1} (or 107 133 ppm) is a standard (representative) concentration for synthesizing an offshore Newfoundland reservoir brine (of the Hibernia oilfield) used in the Hibernia enhanced oil recovery laboratory at Memorial University. The uncertainty of the brine concentration for each salinity is within the range of (−0.4%, +0.4%).

salt	composition (%)	fresh	moderate	high	ocean brine	reservoir brine
$NaCl_{(s)}$	84.4	0 g	5.91 g	17.7 g	29.5 g	90.4 g
$CaCl_2 \cdot 2H_2O_{(s)}$	12.3	0 g	0.86 g	2.6 g	4.3 g	13.202 g
$MgCl_2 \cdot 6H_2O_{(s)}$	2.6	0 g	0.18 g	0.54 g	0.9 g	2.8 g
$KCl_{(s)}$	0.4	0 g	0.03 g	0.08 g	0.14 g	0.4 g
$Na_2SO_{4(s)}$	0.3	0 g	0.02 g	0.07 g	0.11 g	0.345 g
total (g kg^{-1})	—	**0**	**7.0**	**21.0**	**35.0**	**107.133**
total (ppm)	—	**0**	**7000**	**21 000**	**35 000**	**107 133**
total (mol l^{-1})	—	0	0.11	0.33	0.54	1.7

3D bubble sizes. The application of TIR for bubble-scale imaging has been demonstrated in previous studies [37,38], and similar devices have been commercially available (e.g. Foamscan (Teclis Scientific) and Dynamic Foam Analyzer (KRUSS)). Unlike these commercial devices, our approach provides flexibility in container size. A key feature in our study is that we carry out simultaneous measurements on both the macroscopic (bulk) and bubble scales.

2.2. Preparation of saline foams

The aqueous foaming solutions used in this study consist of five salts in a ratio of concentrations designed to create a synthetic mimic of ocean brine. Each of the saline foams was prepared with 50 ml of a solution containing 0.0047 ± 0.0002 mol l^{-1} of Triton X-100 (Fisher Scientific), a commonly used non-ionic surfactant in engineering and biological research laboratories. In actual field trials, the choice of whether to use an ionic and/or non-ionic surfactant depends on the type of rock; non-ionic surfactants such as Triton X-100 are used in any case as co-surfactants because they do not adsorb to the rock surface [39]. The surfactant concentration was chosen to be 0.3 wt% (weight percentage) above its first critical micellar concentration (CMC) of 0.25 mM in the absence of the synthetic ocean brine salts. This CMC value was chosen from a reported range of 0.19–0.27 mM from several studies [40–44]. Even in saline solutions, the surfactant concentrations are safely above the CMC, as the CMC is reported to be lowered in the presence of salts, by as much as 50% for NaCl, and less than 20% for divalent salts [45], per 1 wt% of salt. The 50 ml solution volume was chosen to maximize the use of the uniform column of the bottle and to keep the foam from exceeding the 14 cm limit of the bottle for all salinities. The brine compositions of the foaming solutions are shown in table 1.

2.3. Image analysis

To process each image for the macroscopic foam height analysis, each frame of a given image sequence (i.e. a video) is subtracted from the last frame of the video. We also select a region of interest (ROI), as shown in figure 2 (left), to avoid the edge regions of the bottle being included in our analysis, as there is a small metric ruler attached vertically to the outer front surface of the bottle (not shown), close to one of the edges for a pixel-to-metric conversion. The processed image is a background-subtracted image, of which the pixel intensity reflects the number of scattering events that occur at the liquid–air interfaces in the bulk foam, as the light passes through the crossed polarizers of the macroscopic imaging set-up. To obtain each intensity profile from a macroscopic foam image, as shown in figure 2 (right), we first compute the average of the pixel intensities across the width (horizontal) pixels of the ROI. We then plot the averaged intensity of the width pixels (bottom axis, figure 2 (right)) against the height pixels (left axis, figure 2 (right)) in the direction of gravity.

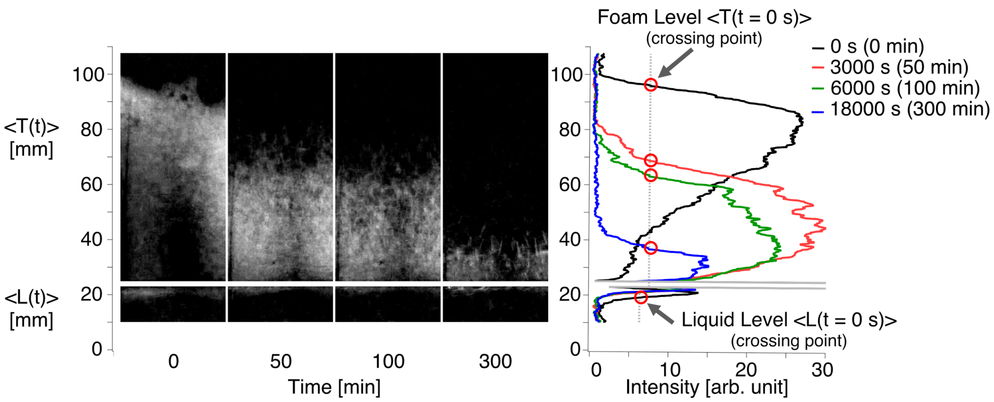

Figure 2. Macroscopic foam analysis. Sample snapshots of background-subtracted macroscopic foam images from one of the four replicates of the foam drainage experiment at a salinity of 7 g kg^{-1} (left) and the corresponding intensity profiles (right) are shown at selected times: $t = 0$ s (0 min), 3000 s (50 min), 6000 s (100 min) and 18 000 s (300 min). Left: A cloudy white colour indicates the foam in the bottle. The upper black region seen in the images indicates a region of no foam, while a slightly lower black region (e.g. between 70 and 80 mm in the image of 50 min), where the white signals (resulting from light scattering) are present, corresponds to a region of a very dry foam. The white stripe added through the images between 21 and 24 mm corresponds to the final liquid meniscus level. Image brightness has been adjusted for visualization purposes. Right: The intensity profiles correspond to the unadjusted version of the images, and the horizontal grey solid lines correspond to the final liquid meniscus level present in the left images. The top common threshold level (shown with a vertical grey dotted line) intersecting with each of the intensity profiles determines the foam level ($\langle T(t)\rangle$) for the upper region of the image (above the final liquid meniscus level). Similarly, another common threshold level is drawn to determine the liquid level ($\langle L(t)\rangle$) for the lower region. Red circles indicate the crossing points that are used to determine the foam and liquid levels. A movie is provided for visualization of the macroscopic-scale dynamics of the foam in electronic supplementary material, video S1. Sample: 4.7 mM of Triton X-100 surfactant in a 7 g kg^{-1} synthetic brine solution.

3. Results

We investigated aqueous saline foams at five different salinities during their free drainage by simultaneously measuring the foam's macroscopic and bubble-scale features.

3.1. Macroscopic-scale foam imaging

We measure the height of a foam in a French square glass column bottle from images obtained from macroscopic-scale imaging, as shown in figure 1. For varying salinities, individual height measurements are obtained from a series of intensity profiles with two different threshold values above noise levels for the upper and the lower region, splitting the height measurements between above and below the final liquid meniscus level. While we introduce two different threshold values for the two regions based on noise level differences, the difference is small. Four intensity profiles are shown for selected times $t = 0$ s (0 min, black), 3000 s (50 min, red), 6000 s (100 min, green) and 18 000 s (300 min, blue) in figure 2. The top of the liquid, i.e. the liquid 'level' $L(t)$, is easily identified by a sharp dip (notch) in the intensity. A white (horizontal) stripe is drawn on each image to delineate regions of liquid from foam (figure 2, left), corresponding to the solid grey horizontal lines seen roughly between 21 and 24 mm (figure 2, right). The top of the foam, i.e. the foam 'level' $T(t)$, is defined by a threshold intensity level that is determined to be just above the background noise seen both in the images by eye and in the intensity profiles (i.e. the minimum threshold level that does not interfere with the foam height measurements across all trials of the experiment). This is shown in the right panel of figure 2, with a set of grey dotted vertical lines through the intensity profiles. These 'common' threshold levels are consistently applied in the analysis of macroscopic foam images from all trials of the experiment.

The time evolution of the foam is shown with the foam level $T(t)$ and the liquid level $L(t)$, at different salinities, in figure 3 (left). Results for each salinity are obtained from the mean of four trials, shown in the main panel of figure 3 (left). The top panel in figure 3 (left) shows the standard deviation of the foam level from the four trials. The initial increase in liquid level for each salinity in figure 3 (left) is re-plotted between 0 and 500 s in electronic supplementary material, figure S2 (top). Three time regimes of foam behaviour are observed. First, there is a rapid decrease in foam level, likely resulting from liquid draining through Plateau borders of the foam (i.e. foam drainage): we call this regime I. In this regime, foam

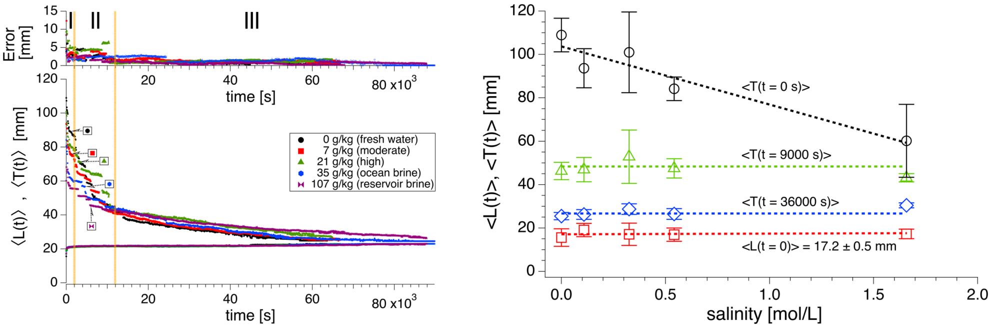

Figure 3. Dependence of macroscopic mean foam and mean liquid levels on salinity. Left: Time dependence of the mean foam level and liquid level for five different salinities. Regimes I, II and III are separated by the yellow vertical lines, where regime I ranges from 0 to 2000 s (33.3 min), regime II ranges from 2000 to 12 000 s (200 min), and regime III ranges from 12 000 s to the rest. The errors (in the top panel) represent the standard deviation of the foam level from all four trials. Right: Mean foam level $\langle T(t)\rangle$ and liquid level $\langle L(t)\rangle$ at $t = 0$ s, 9000 and 36 000 s are plotted against all salinities. The error bars represent the standard deviation of the foam level and liquid level, respectively. $n = 4$ trials.

drainage thins the liquid film separating the larger bubbles at the top of the foam, mainly resulting in rupture events of the top bubbles. Thereafter, one observes sporadic foam collapse events (regime II). Finally, there is a slow decrease in foam level (regime III) with the smallest variations of foam level, which we will examine in more detail shortly. While the top foam surface, which is in contact with the atmosphere, is often not horizontal, the acquisition of four replicates for each salinity and the intensity profile approach to measuring the foam height allows for consistency in our foam height measurements.

Figure 3 (right) shows these results as a dependence of time-dependent foam level, $T(t)$, on salinity at different times. From top to bottom, $t = 0$ s is in regime I, $t = 9000$ s (150 min) is in regime II and $t = 36\,000$ s (600 min or 10 h) is in regime III, with the long-time steady-state liquid level $L(t < 0) \equiv L(t = \infty)$, where t at infinity corresponds to when the foam is completely destroyed and the liquid level is at the same height as before the foam is formed. This long-time steady-state liquid level is obtained in practice from the last frame of each macroscopic-scale video. The liquid level (red squares) across different salinities is relatively flat, indicating that the liquid contribution to the production of foams is independent of salinity, i.e. the difference in initial foam level arises from the incorporation of different volumes of air in the foam. The lowest salinity (fresh water at 0 g kg^{-1} or 0 mol l^{-1}) foaming solution produced foams with the highest initial mean foam level $\langle T(t = 0)\rangle$, while the highest salinity (reservoir brine at 107 g kg^{-1}) foaming solution produced the lowest $\langle T(t = 0)\rangle$. These differences due to salinity become smaller in regime II and smaller yet in regime III. Specifically, while low-salt solutions are significantly more foamable (as seen in the $t = 0$ s data in figure 3 (right)), this has little impact on the long-term survival of the foam. In fact, as seen in the next section, it is the highest-salinity foams that persist at the longest times. The effect of salinity on the initial foam can be quantified in terms of liquid fraction, which can be estimated with the measurements of the initial mean liquid level $\langle L(t = 0\ \mathrm{s})\rangle$ obtained for each salinity. The liquid fraction (defined in electronic supplementary material, section B) is the amount of liquid contained in a bulk foam. Since the liquid contribution to the production of foams is relatively similar across all salinities in our case, the greater the difference between the initial mean foam level $\langle T(t = 0\ \mathrm{s})\rangle$ and the initial mean liquid level $\langle L(t = 0\ \mathrm{s})\rangle$, the lower the initial mean liquid fraction. As shown in electronic supplementary material, figure S2 (bottom), the highest-salinity (i.e. 107 g kg^{-1}) foams show the highest initial mean liquid fraction, while the initial mean liquid fraction of the other foams (i.e. 0–35 g kg^{-1}) is generally lower and within the uncertainties of one another.

3.2. Logarithmic decrease in foam height: long-time behaviour of the foam

Time evolution of the difference between the mean foam level $\langle T(t)\rangle$ and the mean liquid level $\langle L(t)\rangle$ is plotted in figure 4 (left) for each salinity, which we define as the (time-dependent) mean 'foam height' ($\langle F(t)\rangle = \langle T(t)\rangle - \langle L(t)\rangle$). It is noticeable that regime III is characterized by a decrease in foam height that is linear in the logarithm of the time elapsed, a result also noted in the experiments of Iglesias *et al.* [47]. One can characterize the logarithmic dependence of the foam through the form

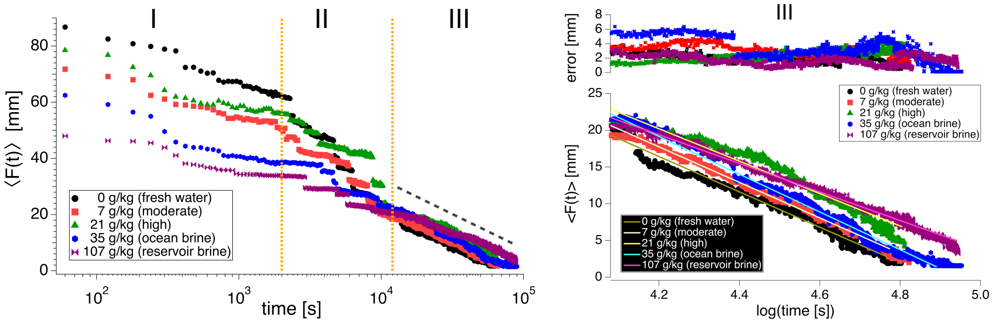

Figure 4. Logarithmic decrease of mean foam height. Left: Long-time behaviour of the mean foam height $\langle F(t)\rangle$, for different salinities, exhibits a logarithmic decrease in regime III. Regimes I, II and III are separated by the yellow vertical lines, where regime I ranges from 0 s to 2000 s (33.3 min), regime III is the logarithmic regime, which begins around 12 000 s (200 min) and regime II, which is in between, exhibits the foam collapse events. Right: The mean foam height of each salinity in regime III is shown along with a fit in the form of equation (3.1). The errors in the top panel show the standard deviation of the foam height from all four trials of each salinity.

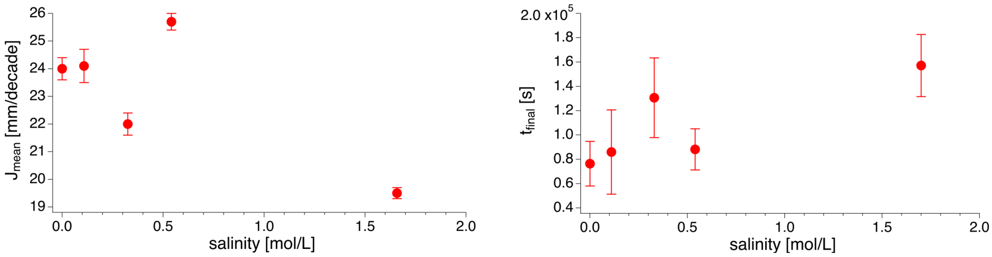

Figure 5. Salinity dependence of J_{mean} (the mean foam height reduction rate, left) and t_{final} (the time for the macroscopic foam to reach the liquid meniscus level, right). Results are shown for the logarithmic decrease regime (regime III). The error bars on J_{mean} represent the standard deviation of J_{mean} obtained from the weighted fits of the form of equation (3.1), as shown in figure 4 (right) and electronic supplementary material, figure S7 (left). The error bars on t_{final} are computed using the errors of $\langle F(1)\rangle$ and J_{mean} from the fits.

$$\langle F(t)\rangle = \langle F(1)\rangle - J_{\text{mean}} \log_{10}(t) = -J_{\text{mean}} \log_{10}(t/t_{\text{final}}), \tag{3.1}$$

where $\langle F(1)\rangle$ is the extrapolated foam height at 1 s, and J_{mean} (in units of mm/ $\log_{10}(t)$ or mm decade^{-1}) is the decrease in foam height per decade of time. The y-intercept of the linear relationship in equation (3.1) (i.e. $\langle F(1)\rangle$) is less physically meaningful than the x-intercept that can be obtained from the same linear relationship (i.e. $\langle F(1)\rangle/J_{\text{mean}}$), which can be interpreted as $\log_{10}(t_{\text{final}})$ because it is the time when the foam height is reduced to zero. Figure 4 (right) re-plots just the data in regime III. The long-time foam height $\langle F(t)\rangle$ in regime III is instructive: data for all salinities converge, with the exception of the highest salinity foam made at a salt concentration that is intended to mimic the salinity of reservoir brine, which persists for the longest times. All salinities converge at the start of regime III, as can be seen, but the highest salinity foam decays noticeably slower than the rest of the salinities. In the literature, the half-life time $t_{1/2}$ is often used as a measure of foam stability. Given the clearly non-exponential decay of the foam, $t_{1/2}$ is not very meaningful, and we examine instead the long-time persistence of the foam directly.

A fit of figure 4 (right) to equation (3.1) yields the mean foam height reduction rate J_{mean} and the time to final collapse t_{final}. Figure 5 (left) shows J_{mean} as a function of salinity. It is seen, quite clearly, that it is significantly lower at the highest salinity. The time to final collapse t_{final}, which is plotted as a function of salinity in figure 5 (right), shows a steady increase with increasing salinity. These observations can be corroborated with the analysis of the images at bubble scale, which is discussed in the next section.

3.3. Bubble-scale foam imaging

Focusing on a fixed ROI, we examine bubble size evolution as a function of time. Figure 6 shows an example of bubble size evolution as a function of time for a foam of salinity 7 g kg^{-1}. The bottom of the ROI is always at a height of 30 mm from the base of the bottle, and thus always above the final liquid level of

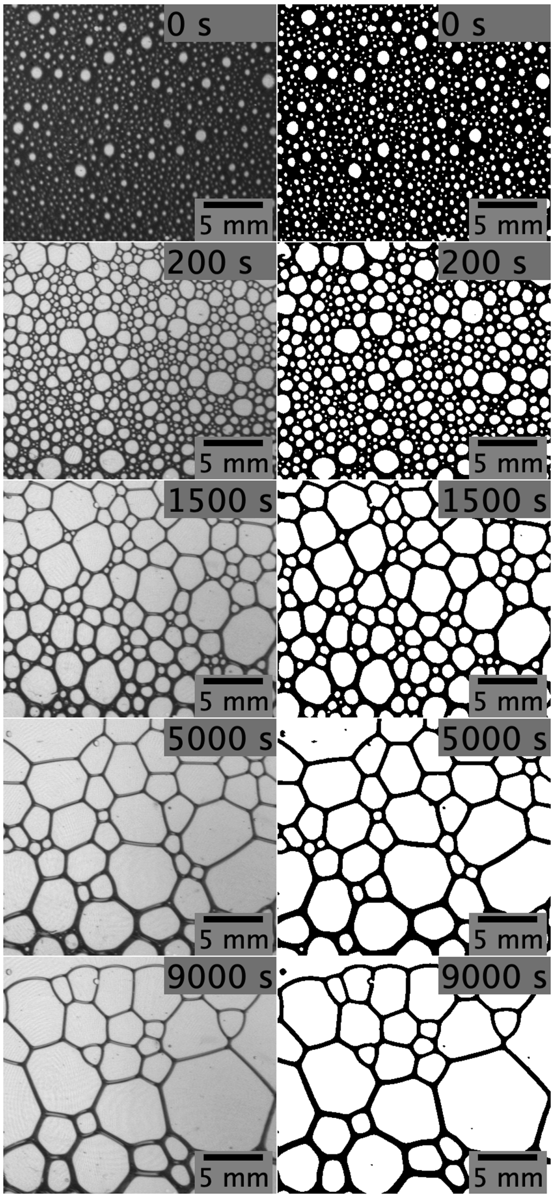

Figure 6. Bubble-scale images. A set of perspective distortion-corrected raw images for different times (left) and the corresponding processed binarized images (right) is shown. The bubble sizes are obtained from the processed images, excluding the edge bubbles. A time-dependent visualization of the bubble-scale dynamics of the foam for up to 10 000 s is shown in electronic supplementary material, video S2. Sample: CMC + 0.3 wt% (0.0047 ± 0.0002 mol l^{-1}) of Triton X-100 surfactant in a 7 g kg^{-1} synthetic brine solution (total volume = 50 ml).

23 mm, as can be seen in figure 2. The selected ROI is a rectangle, 23 mm in lateral extent and 20 mm vertically. The images are corrected for perspective distortion, as described in the electronic supplementary material (see the discussion in electronic supplementary material, figure S3).

The corrected raw images for bubble-scale foam evolution are shown at five different times (figure 6, left panel). Corresponding binarized images of the corrected raw images are shown in the right panel of figure 6. These binarized images are then used to extract the mean bubble size (by measuring the bubble cross-sectional area) as a function of time. While one could also measure bubble size distributions, the statistics are not sufficient to make any concrete interpretations of the overall pattern of our bubble-scale results. We will address this in future work.

The bubble sizes evolve in time (top to bottom in figure 6) from the sub-millimetre length scale to the millimetre length scale. Qualitatively, we are at the onset of a transition from circular bubbles to faceted bubbles with Plateau borders at t = 1500 s. This timescale coincides with our previous identification (in macroscopic-scale foam images) of a transition from regime I, with a rapid decrease in mean

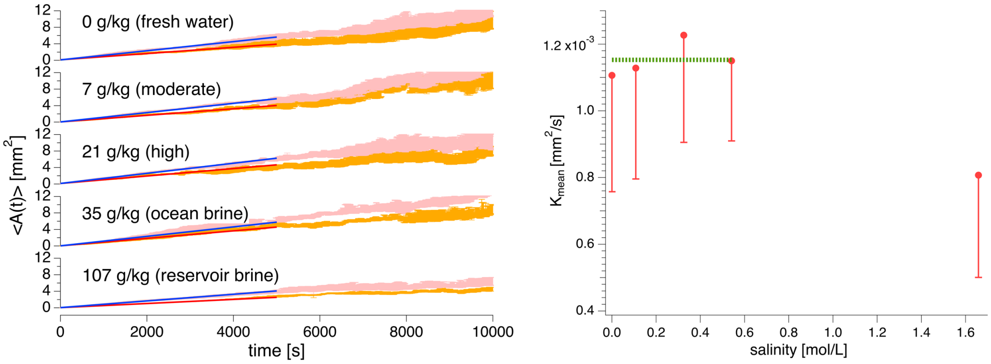

Figure 7. Salinity dependence of the growth rate of the mean bubble cross-sectional area. Left: The time evolution of mean bubble area (pink: full ROI; orange: bottom half of ROI) is fitted to a linear function, $\langle A(t)\rangle = \langle A_0\rangle + K_{\text{mean}}t$, over the 5000 s range (blue: full ROI; red: bottom half of ROI). Right: A set of the mean bubble area growth rates K_{mean} obtained from the full ROI images over the first 5000 s is plotted for each salinity. The one-sided error bars represent the difference between the K_{mean} obtained from the full ROI and the K_{mean} obtained from the bottom half of the full ROI. For a guide to the eye, the dotted line in green shows an average of the K_{mean} values for the first four salinities (i.e. 1.15×10^{-3} mm^2 s^{-1}). $n = 4$ trials.

foam height (approximately a 30% decrease in foam height over 2000 s), to regime II, where there is a slow decrease in mean foam height coupled with sporadic foam collapse events. By this time, most of the foam drainage is complete, and regime II can be identified as the regime of slower phenomena, coalescence and coarsening. The time regime corresponding to regime III in the previous discussion is probed in the bubble-scale study, but it is already seen in the bottom panel of figure 6, at $t = 9000$ s (150 min), that there are fewer bubbles detected in the ROI. Edge bubbles are not counted. The statistics become poor past $t = 20\,000$ s (333.3 min or 5.5 h). Detected bubble counts for the individual trial data are available in electronic supplementary material, figures S4 and S5.

In figure 6, at any instant, there is a spatial variation in liquid fraction across the ROI and can largely be divided into two parts: the upper half and the bottom half of the ROI for bubble size measurements. In order to account for measurement error on the growth rate of the bubbles in the full ROI due to this variation in liquid fraction, the same bubble analysis is performed to obtain the growth rate of the mean bubble area for the bottom half of the ROI. We compute the difference of the mean bubble area growth rates from the full ROI and the bottom-half ROI for each salinity and use this as a one-sided error, as shown in figure 7 (right). In figure 8, we show a sample bubble size analysis of the time evolution of mean bubble cross-sectional area, comparing the full ROI and the bottom-half ROI at a salinity of 7 g kg^{-1}. The mean values are obtained from the average of four trials over the first 10 000 s. Qualitatively, the time evolution of bubble size for each trial is similar to the evolution shown in figure 6. The initial mean bubble cross-sectional area $\langle A_0\rangle$ is approximately 0.07 mm^2 for the full ROI of this salinity. Both $\langle A_0\rangle$ and the time-dependent mean bubble area $\langle A(t)\rangle$ are shown for all salinities in electronic supplementary material, figure S6. It is seen that the bubble growth in the full ROI is linear from a few seconds to $t = 5000$ s for all trials of all salinities. Indeed, as shown in figure 8 as an example, an average over four trials also shows a reasonable agreement with a linear growth law all the way to $t = 5000$ s, which we choose as a reasonable range for the analysis across all the salinities. While noisier for longer times, we show the data for all trials of all salinities, all the way to $t = 10\,000$ s in electronic supplementary material, figure S7 (right column), and to $t = 20\,000$ s in electronic supplementary material, figures S4 and S5.

A linear growth of average bubble area is indeed consistent with previous experiments in 2D and 3D foams, where a $t^{1/2}$ dependence of the bubble diameter was observed, corresponding to a linear-t dependence of the bubble area (in 2D) and of the cross-sectional area (in 3D) [35]. The von Neumann law for domain coarsening predicts, in two dimensions, that for each individual bubble cell,

$$\mathrm{d}A/\mathrm{d}t = K, \tag{3.2}$$

where $K = (2\pi/3)\gamma\kappa(n - 6)$ is the bubble area growth rate. n is the number of sides of each bubble, γ is the surface tension (in units of J m^{-2}) of the bubble wall, and κ is the permeability constant for the bubble film. Equation (3.2) was formulated for each individual bubble in a 2D foam, but an averaged $\langle A\rangle \propto t$ growth law appears to hold experimentally, and even in 3D foams [35,38,48]. The surface tension γ is very weakly salinity-dependent, as has been measured (see electronic supplementary material, figure S8). If coarsening through gas diffusion dominates over film rupture events, then the permeability constant κ

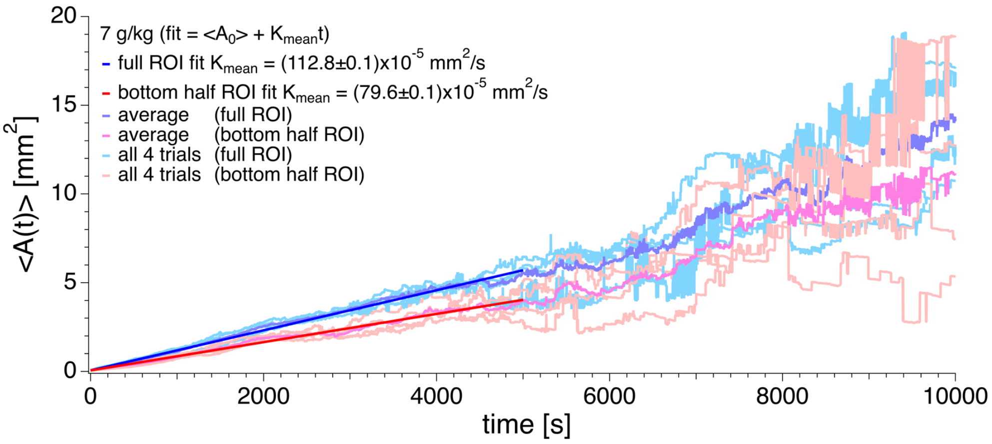

Figure 8. Growth of mean bubble cross-sectional area. The time evolution of the mean bubble cross-sectional area in the full ROI and the bottom-half ROI is shown for all trials of the 7 g kg^{-1} foam. Individual trials (independent replicates) are shown in light blue and light pink for the full ROI and the bottom-half ROI, respectively. The average (purple) of all trials of the full ROI is fitted (blue) to a linear function as shown in the legend. Similarly, the fit (red) of the average (dark pink) of all trials for the bottom-half ROI is also shown over the same range of the first 5000 s.

depends on the gas diffusivity through the foam liquid film, which in turn depends on liquid viscosity (also measured in electronic supplementary material, figure S9, as a function of salinity) and on the solubility of air in brine. While these multiple dependencies are challenging to quantify, it should be noted that both the difference in solubility of air in fresh water and sea water (about 30% less in sea water), and the difference in viscosity of fresh water and sea water (about 10% higher in sea water) point to a steady reduction in $\varkappa$ (and thus K) with increasing salinity. No corresponding decrease in K_{mean} is seen from 0 to 35 g kg^{-1}. At the highest salinity (107 g kg^{-1}), we have no data for gas solubility, but the viscosity is enhanced by over 20%. Here, K_{mean} is reduced by 40%. The fact that it is reduced is reasonable; with what we know, we cannot justify the magnitude of the decrease.

Using the average of four trials, we find linear dependence on bubble area for all salinities: this is shown in figure 7 (left). Fitting the time-dependent mean bubble area to the form $\langle A(t)\rangle = \langle A_0\rangle + K_{\text{mean}}t$, the slopes yield the mean bubble growth rates K_{mean}, which we plot as a function of the salinity, as shown in figure 7 (right). Consistent with the observation for the long-time bubble areas, K_{mean} is seen to be roughly 1.15×10^{-3} mm^2 s^{-1} for salinities from 0 to 35 g kg^{-1} (0–0.54 mol l^{-1}), but roughly half of that value for the 107 g kg^{-1} salinity (1.66 mol l^{-1}) foam. Since the surface tensions for all salinities are not very different (less than 2%; see electronic supplementary material, figure S8), the difference in K_{mean} for the highest salinity must arise from differences in the permeability constant $\varkappa$ which will vary more significantly due to the appreciable change in the fluid viscosity (see electronic supplementary material, figure S9).

4. Discussion and conclusion

In this work, we developed an imaging system that could simultaneously visualize the dynamics of aqueous foams, both at the macroscopic scale and at the bubble scale, in an automated way across multiple timescales. Our system is flexible and designed to enable measurements that span from seconds to an entire day. Finally, the system was used to examine the decay of the foam as a function of salinity. For our study, we investigated the evolution of 3D aqueous foams in the presence of non-ionic surfactant (4.7 mm of Triton X-100) and synthetic ocean brine at five different salinities. While the effect of electrolyte solutions and seawater on surfactant foams has been examined in other studies [26,27], we have focused on a systematic study of the time dependence of saline foams at different salinities.

4.1. Macroscopic-scale measurements

At the macroscopic scale, we followed the evolution of foam height for approximately up to 25 h. We observed three time regimes of behaviour. In regime I, between 0 and 2000 s (33.3 min), rapid foam drainage caused the foam height to decrease for all salinities. While bubble coalescence events were likely also happening here, the first 500 s were dominated by liquid drainage in the foam (see electronic supplementary material, figure S2 (top)). In regime II, between 2000 and 12 000 s (200 min), foam collapse events were frequently observed. In regime III, all saline foams converged in foam height at around 12 000 s, after which the rate of decrease in foam height qualitatively seemed similar, but with one exception: the foams with the highest salinity brine (i.e. the salinity corresponding to reservoir brine) survived longer than the rest on average, as shown most clearly in figure 4 (right). A quantitative comparison with the J_{mean} of all salinities in figure 5 confirmed that the reservoir brine foams had the slowest rate of decrease in foam height in regime III. While it is typical in many studies to quantify a foam's lifetime by measuring the height or volume of its half-life time (i.e. the time it takes for the foam to reach half its initial height or volume in the case of our bottle or containers alike) [11,24,49], in our study, we probed much longer times. Indeed, the half-life time for our foams is in regime II (i.e. it is not yet in regime III, where there is logarithmic decrease in foam height). Thus, the half-life does not capture all of the physics of the decrease of foam height. It is, however, reasonable to question whether this slower rate of decrease at the highest salinity is significant; this point is addressed below in connection with the bubble-scale measurements.

For all salinities, the foam height in regime III exhibits a slow, logarithmic decrease, as shown in figure 4. What is the origin of the logarithmic height relaxation of the foam? Logarithmic time dependence (or shear rate dependence) has been observed in a wide range of systems: examples are settling in a sandpile [50], stresses in sheared granular materials [51,52], excess conductance in electron glasses [53,54], the height of crumpled Mylar films [52,54,55] and stresses in a settling elastic foam [52]. Typical relaxations in simple systems are exponential, with a single relaxation rate. Amir *et al.* [54] model logarithmic relaxations in granular systems as arising from a probability distribution $P(f)$ (of relaxation rates f) that obeys a $1/f$ frequency dependence. We propose, therefore, that the logarithmic relaxation of foam heights observed at long times independent of salinity arises from a generic property of granular materials. Indeed, it has been noted that foam is a particular kind of granular material [56], and the observed logarithmic relaxation in our experiments is good evidence for this. The measured foam height reduction rate J_{mean} is significantly lower for the highest-salinity (reservoir brine) foam, and the time to final collapse t_{final} increases with salinity.

A practical outcome of our macroscopic-scale measurements is that the foam with highest salinity (i.e. with a salinity corresponding to reservoir brine) exhibits both the weakest foamability (seen clearly in figure 3 (right) where the initial foam height of the highest salinity foam is the smallest) but it also persists the longest (seen in figure 4 (right)). It is only fair to point out, however, that the most saline foam only outlives those of lower salinity when 80% (or more) of the foam is already gone. We note that this unexpected behaviour occurs in the logarithmic decay regime identified in this work.

4.2. Bubble-scale measurements

At the bubble scale, we probed the foam for 20 000 s (333.3 min). During the first 5000 s (83.3 min), the number of bubbles in the field of view was adequate for obtaining statistical information on bubble sizes in all trials of each salinity. In all cases, the ROI for the bubble-scale measurements was chosen at the same absolute position of 30 mm from the base of the bottle. In all the regimes identified for macroscopic-scale imaging (as defined for the macroscopic-scale dynamics), the mean cross-sectional area of the bubbles (in the ROI) increased steadily with time for all salinities. Perhaps surprisingly, the foams showed classical von Neumann scaling at all salinities: the mean bubble cross-sectional area grew linearly with time. This might indicate that in spite of the fact that we observe a coexistence of coalescence and diffusive coarsening, the latter is dominant, at least at the bottom of the foam. The growth rates were reasonably consistent for all salinities, with the lone exception of the highest salinity: the foaming solution with salinity corresponding to reservoir brine. An important point to revisit is with regard to high long-time persistence of the foam at the highest salinity (i.e. salinity comparable with reservoir brine).

4.3. Comparison between scales

At the macroscopic scale, approximately 90 000 s of data (25 h) were required to show clearly that the highest salinity foam of 107 g kg^{-1} was the most persistent. For the bubble scale, however, a clear difference in growth rates of the mean bubble cross-sectional area, K_{mean}, is seen already at very early times. Figure 9 shows that through both macroscopic (t_{final}) and bubble-scale (K_{mean}) measures, the foam made from reservoir brine stands out as longest-lasting and most stable. K_{mean} shows very little change as a

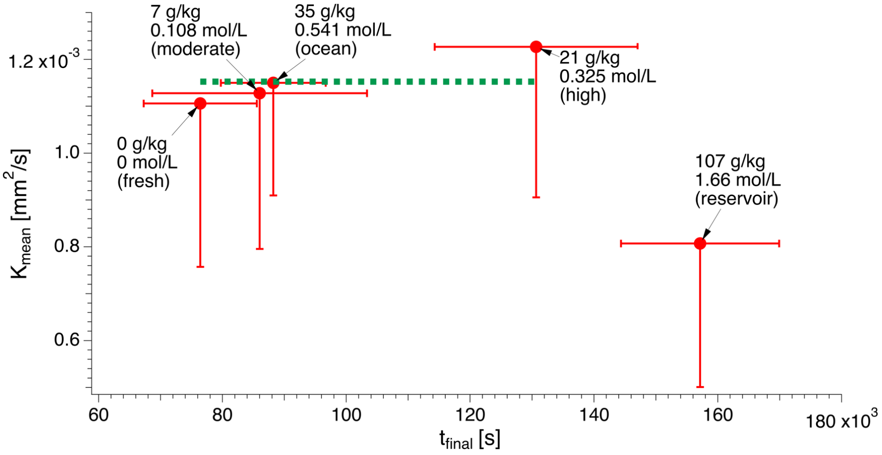

Figure 9. Comparison between the macroscopic and bubble scales. The bubble-scale K_{mean}, within errors, does not change much with increase in t_{final}, with the exception of the highest salinity, where there is a drop in K_{mean}. The error bars on the K_{mean} reflect the uncertainties obtained from the difference between the K_{mean} obtained from the full ROI and the K_{mean} from the bottom-half ROI. The dotted line in green shows that the average K_{mean} of the first four salinities (i.e. 1.15×10^{-3} mm^2 s^{-1}) is significantly higher than the value at highest salinity. $n = 4$ trials.

function of salinity except for the highest salinity (reservoir brine). The bubble area at a fixed reference above the unperturbed liquid level is also much less susceptible to the 'noise' in foam height that arises from the foam collapse events. Thus, we conclude that bubble-scale imaging is a more sensitive probe of foam stability.

4.4. The long-time behaviour of reservoir brine foams

What characteristic of the reservoir brine makes foams made from it persist for longer times? In the absence of surfactant, a critical salt concentration has been proposed above which bubble coalescence is inhibited [23]: experimentally, this concentration is of order 0.1–0.3 mol l^{-1} [23,57,58] for some of the salts used in this study. In the presence of a non-ionic surfactant, we see a significant change in behaviour at about 0.5 mol l^{-1}. The physical properties of the foaming solution could provide some clues: to this end, we measured the surface tension (electronic supplementary material, figure S8), viscosity (electronic supplementary material, figure S9) and density (electronic supplementary material, figure S10) of the foaming solutions. The surface tension shows only a slight decrease at the highest salinity. The density and viscosity show a systematic increase of 6% and 17%, respectively. It is possible that the approximately 17% increase in viscosity at the highest salinity contributes to the increased stability, but specific salt effects at the air–water interface could also be at play. Future work will focus on studies (using another technique such as X-ray tomography [59]) to image foams in 3D and also at several intermediate salinities to understand the behaviour of the highest salinity foam further. While our work has focused on a non-ionic surfactant, we have not yet touched on the very interesting question, addressed in part by other groups, of how foams made with ionic surfactants would behave over the entire decay process [24,60,61]. Barring the observation of Iglesias *et al.* [47], these studies, however, have not examined long-time foam persistence in the systematic way as we describe in this work: identifying different foam decay regimes and, in particular, the existence of a logarithmic decay regime at long times. Examining the rheological properties of these foams [62–66] is also of interest for future work.

4.5. Relevance to oil recovery

The unexpected long-term persistence of high-salinity foams (albeit in the newly identified logarithmic decay regime after a significant fraction of the foam has already collapsed) is potentially good news for oil recovery applications with the provision that the mechanisms for foam collapse in bulk and porous media can be quite different [67]. However, it should be noted that the next steps involve the survival of this foam inside porous rock [68], where coarsening is only unrestricted until the bubbles grow to the size of the pores. Since our study, at long times, focuses on the bottom of the foam where capillary effects are more important, there is hope that some of our results may carry over to porous rock, where capillary pressure effects are likely more important than gravity effects. In addition, foam studies for enhanced oil recovery will need to contend with variable electrostatic properties [39] that will likely require mixed (ionic and non-ionic) surfactants.

4.6. Significance

The main contribution of this work is a quantitative examination on two length scales of saline foams. We find, remarkably, that the bubble-scale probe (at the bottom of the foam) is an early warning of the long-time behaviour of the foam studied on the bulk (macroscopic) scale. Moreover, the long-time persistence of the foam turns out, quite universally for all salinities, to be logarithmic. We believe this is significant because past quantitative measures of foam lifetime (such as the half-life) are predicated on an exponential (not logarithmic) decay model. We thus hope that the methods presented in this work will be found to be broadly applicable for different foam systems (saline or not).

Ethics. This work did not require ethical approval from a human subject or animal welfare committee.

Data accessibility. Data analysis files for graphs plotted using the software package Igor Pro (Wavemetrics Inc.) are included as electronic supplementary material [69].

Declaration of AI use. We have not used AI-assisted technologies in creating this article.

Authors' contributions. T.I.: formal analysis, investigation, methodology, validation, visualization, writing—original draft, writing—review and editing; L.A.J.: funding acquisition, investigation, methodology, project administration, resources, writing—review and editing; A.Y.: conceptualization, formal analysis, funding acquisition, investigation, methodology, project administration, supervision, writing—review and editing.

All authors gave final approval for publication and agreed to be held accountable for the work performed therein.

Conflict of interest declaration. We declare we have no competing interests.

Funding. The authors thank Natural Sciences and Engineering Research Council of Canada (A.Y. acknowledges NSERC RGPIN-2019-04970 and RGPIN-2025-05494), Chevron Canada Ltd, Hibernia Management and Development Company (HMDC), Energy Research and Innovation Newfoundland and Labrador (ERINL), Innovate NL (formerly RDC), Mitacs and the Canadian Foundation for Innovation (CFI) for financial support.

Acknowledgements. We thank our colleagues in the Soft Materials group (www.softmaterials.ca) and the Hibernia EOR Research Group, especially Mr Edison Sripal for providing technical and safety training in the Hibernia EOR laboratory. We also thank Mr Gordon Whelan (physics machine shop) for technical support and Dr Jinesh Machale for helpful comments. A.Y. thanks Dr Kabir Ramola (TIFR-Hyderabad) for valuable discussions.

References

1. Hilgenfeldt S, Koehler SA, Stone HA. 2001 Dynamics of coarsening foams: accelerated and self-limiting drainage. *Phys. Rev. Lett.* **86**, 4704–4707. (doi:10.1103/PhysRevLett.86.4704)
2. Vera MU, Durian DJ. 2002 Enhanced drainage and coarsening in aqueous foams. *Phys. Rev. Lett.* **88**, 088304. (doi:10.1103/PhysRevLett.88.088304)
3. Cohen-Addad S, Höhler R, Khidas Y. 2004 Origin of the slow linear viscoelastic response of aqueous foams. *Phys. Rev. Lett.* **93**, 028302. (doi:10.1103/PhysRevLett.93.028302)
4. Briceño-Ahumada Z, Drenckhan W, Langevin D. 2016 Coalescence in draining foams made of very small bubbles. *Phys. Rev. Lett.* **116**, 128302. (doi:10.1103/PhysRevLett.116.128302)
5. Forel E, Dollet B, Langevin D, Rio E. 2019 Coalescence in two-dimensional foams: a purely statistical process dependent on film area. *Phys. Rev. Lett.* **122**, 088002. (doi:10.1103/PhysRevLett.122.088002)
6. Arzhavitina A, Steckel H. 2010 Foams for pharmaceutical and cosmetic application. *Int. J. Pharm.* **394**, 1–17. (doi:10.1016/j.ijpharm.2010.04.028)
7. Fitzgerald K, Stephan SB, Ma N, Wu QV, Stephan MT. 2024 Liquid foam improves potency and safety of gene therapy vectors. *Nat. Commun.* **15**, 4523. (doi:10.1038/s41467-024-48753-9)
8. Hill C, Eastoe J. 2017 Foams: from nature to industry. *Adv. Colloid Interface Sci.* **247**, 496–513. (doi:10.1016/j.cis.2017.05.013)
9. Yan W, Miller CA, Hirasaki GJ. 2006 Foam sweep in fractures for enhanced oil recovery. *Colloids Surf. A* **282–283**, 348–359. (doi:10.1016/j.colsurfa.2006.02.067)
10. Nguyen P, Fadaei H, Sinton D. 2014 Pore-scale assessment of nanoparticle-stabilized CO_2 foam for enhanced oil recovery. *Energy Fuels* **28**, 6221–6227. (doi:10.1021/ef5011995)
11. Osei-Bonsu K, Shokri N, Grassia P. 2015 Foam stability in the presence and absence of hydrocarbons: from bubble- to bulk-scale. *Colloids Surf. A* **481**, 514–526. (doi:10.1016/j.colsurfa.2015.06.023)
12. Grassia P. 2021 Surfactant transport between foam films. *J. Fluid Mech.* **928**, F1. (doi:10.1017/jfm.2021.690)
13. Cantat I, Cohen-Addad S, Elias F, Graner F, Höhler R, Pitois O, Rouyer F, Saint-Jalmes A. 2013 *Foams: structure and dynamics*. Oxford, UK: Oxford University Press.
14. Sabet N, Hassanzadeh H, De Wit A, Abedi J. 2021 Scalings of Rayleigh-Taylor instability at large viscosity contrasts in porous media. *Phys. Rev. Lett.* **126**, 094501. (doi:10.1103/PhysRevLett.126.094501)

15. Dias EO, Alvarez-Lacalle E, Carvalho MS, Miranda JA. 2012 Minimization of viscous fluid fingering: a variational scheme for optimal flow rates. *Phys. Rev. Lett*. **109**, 144502. (doi:10.1103/PhysRevLett.109.144502)
16. Zheng Z, Kim H, Stone HA. 2015 Controlling viscous fingering using time-dependent strategies. *Phys. Rev. Lett*. **115**, 174501. (doi:10.1103/PhysRevLett.115.174501)
17. Coutinho ÍM, Miranda JA. 2020 Control of viscous fingering through variable injection rates and time-dependent viscosity fluids: beyond the linear regime. *Phys. Rev. E* **102**, 063102. (doi:10.1103/PhysRevE.102.063102)
18. Craig VSJ, Ninham BW, Pashley RM. 1993 Effect of electrolytes on bubble coalescence. *Nature* **364**, 317–319. (doi:10.1038/364317a0)
19. Tripathi L, Irorere VU, Marchant R, Banat IM. 2018 Marine derived biosurfactants: a vast potential future resource. *Biotechnol. Lett*. **40**, 1441–1457. (doi:10.1007/s10529-018-2602-8)
20. Evans DF, Wennerström H. 1999 *The colloidal domain: where physics, chemistry, biology, and technology meet*, 2nd edn. New York, NY: Wiley-VCH.
21. Weaire DL, Hutzler S. 1999 *The physics of foams*. Oxford, UK: Oxford University Press. (doi:10.1093/oso/9780198505518.001.0001)
22. Ninham BW, Nostro PL. 2010 *Molecular forces and self assembly: in colloid, nano sciences and biology*. Cambridge, UK: Cambridge University Press.
23. Firouzi M, Howes T, Nguyen AV. 2015 A quantitative review of the transition salt concentration for inhibiting bubble coalescence. *Adv. Colloid Interface Sci*. **222**, 305–318. (doi:10.1016/j.cis.2014.07.005)
24. Emami H, Ayatizadeh Tanha A, Khaksar Manshad A, Mohammadi AH. 2022 Experimental investigation of foam flooding using anionic and non-ionic surfactants: a screening scenario to assess the effects of salinity and pH on foam stability and foam height. *ACS Omega* **7**, 14832–14847. (doi:10.1021/acsomega.2c00314)
25. Carey E, Stubenrauch C. 2010 Foaming properties of mixtures of a non-ionic (C12DMPO) and an ionic surfactant (C12TAB). *J. Colloid Interface Sci*. **346**, 414–423. (doi:10.1016/j.jcis.2010.03.013)
26. Castro S, Laskowski JS. 2011 Froth flotation in saline water. *KONA Powder Part. J*. **29**, 4–15. (doi:10.14356/kona.2011005)
27. Laskowski JS, Castro S, Ramos O. 2014 Effect of seawater main components on frothability in the flotation of Cu-Mo sulfide ore. *Physicochem. Probl. Miner. Process.* **50**, 17–29. (doi:10.5277/ppmp140102)
28. Von Neumann J. 1952 Metal interfaces. *Am. Soc. Met. Clevel*. **108**, 108–110.
29. Stavans J. 1990 Temporal evolution of two-dimensional drained soap froths. *Phys. Rev. A* **42**, 5049–5051. (doi:10.1103/PhysRevA.42.5049)
30. Chieco AT, Durian DJ. 2021 Experimentally testing a generalized coarsening model for individual bubbles in quasi-two-dimensional wet foams. *Phys. Rev. E* **103**, 012610. (doi:10.1103/PhysRevE.103.012610)
31. Fortuna I, Thomas GL, de Almeida RMC, Graner F. 2012 Growth laws and self-similar growth regimes of coarsening two-dimensional foams: transition from dry to wet limits. *Phys. Rev. Lett*. **108**, 248301. (doi:10.1103/PhysRevLett.108.248301)
32. Drenckhan W, Saint-Jalmes A. 2015 The science of foaming. *Adv. Colloid Interface Sci*. **222**, 228–259. (doi:10.1016/j.cis.2015.04.001)
33. ASTM International. 2002 *Standard test method for foam in aqueous media (bottle test)*. Technical report. West Conshohocken, PA: American Society for Testing and Materials.
34. Sigma-Aldrich. 2017 *Suggestions for cleaning glassware*. Technical report. Aldrich.
35. Durian DJ, Weitz DA, Pine DJ. 1990 Dynamics and coarsening in three-dimensional foams. *J. Phys. Condens. Matter* **2**, SA433–SA436. (doi:10.1088/0953-8984/2/S/069)
36. Durian DJ, Weitz DA, Pine DJ. 1991 Multiple light-scattering probes of foam structure and dynamics. *Science* **252**, 686–688. (doi:10.1126/science.252.5006.686)
37. Forel E, Rio E, Schneider M, Beguin S, Weaire D, Hutzler S, Drenckhan W. 2016 The surface tells it all: relationship between volume and surface fraction of liquid dispersions. *Soft Matter* **12**, 8025–8029. (doi:10.1039/C6SM01451H)
38. Roth AE, Chen BG, Durian DJ. 2013 Structure and coarsening at the surface of a dry three-dimensional aqueous foam. *Phys. Rev. E* **88**, 062302. (doi:10.1103/PhysRevE.88.062302)
39. Machale J, Majumder SK, Ghosh P, Sen TK. 2020 Role of chemical additives and their rheological properties in enhanced oil recovery. *Rev. Chem. Eng*. **36**, 789–830. (doi:10.1515/revce-2018-0033)
40. Yu D, Huang F, Xu H. 2012 Determination of critical concentrations by synchronous fluorescence spectrometry. *Anal. Methods* **4**, 47–49. (doi:10.1039/C1AY05495C)
41. Lavkush Bhaisare M, Pandey S, Shahnawaz Khan M, Talib A, Wu HF. 2015 Fluorophotometric determination of critical micelle concentration (CMC) of ionic and non-ionic surfactants with carbon dots via Stokes shift. *Talanta* **132**, 572–578. (doi:10.1016/j.talanta.2014.09.011)
42. Anand U, Jash C, Mukherjee S. 2011 Spectroscopic determination of critical micelle concentration in aqueous and non-aqueous media using a non-invasive method. *J. Colloid Interface Sci*. **364**, 400–406. (doi:10.1016/j.jcis.2011.08.047)
43. Sigma-Aldrich. 1999 *Triton X-100 product information*. Technical report. Sigma-Aldrich.
44. Moayedi M. 2015 An experimental study on surfactant-alternating-gas process. Master's thesis, [St John's, Canada]: Memorial University of Newfoundland.
45. Akhlaghi N, Riahi S. 2019 Salinity effect on the surfactant critical micelle concentration through surface tension measurement. *Iran. J. Oil Gas Sci. Technol.* **8**, 50–63. (doi:10.22050/ijogst.2019.156537.1481)
46. US Geological Survey. 2018 Saline water and salinity. See https://www.usgs.gov/special-topics/water-science-school/science/saline-water-and-salinity (accessed 1 February 2026).
47. Iglesias E, Anderez J, Forgiarini A, Salager JL. 1995 A new method to estimate the stability of short-life foams. *Colloids Surf. A* **98**, 167–174. (doi:10.1016/0927-7757(95)03101-I)
48. Glazier JA, Gross SP, Stavans J. 1987 Dynamics of two-dimensional soap froths. *Phys. Rev. A* **36**, 306–312. (doi:10.1103/PhysRevA.36.306)

49. Simjoo M, Rezaei T, Andrianov A, Zitha PLJ. 2013 Foam stability in the presence of oil: effect of surfactant concentration and oil type. *Colloids Surf. A* **438**, 148–158. (doi:10.1016/j.colsurfa.2013.05.062)
50. Leung CF, Lee FH, Yet NS. 1996 The role of particle breakage in pile creep in sand. *Can. Geotech. J.* **33**, 888–898. (doi:10.1139/t96-119)
51. Hartley RR, Behringer RP. 2003 Logarithmic rate dependence of force networks in sheared granular materials. *Nature* **421**, 928–931. (doi:10.1038/nature01394)
52. Lahini Y, Gottesman O, Amir A, Rubinstein SM. 2017 Nonmonotonic aging and memory retention in disordered mechanical systems. *Phys. Rev. Lett*. **118**, 085501. (doi:10.1103/PhysRevLett.118.085501)
53. Orlyanchik V, Ovadyahu Z. 2004 Stress aging in the electron glass. *Phys. Rev. Lett*. **92**, 066801. (doi:10.1103/PhysRevLett.92.066801)
54. Amir A, Oreg Y, Imry Y. 2012 On relaxations and aging of various glasses. *Proc. Natl Acad. Sci. USA* **109**, 1850–1855. (doi:10.1073/pnas.1120147109)
55. Matan K, Williams RB, Witten TA, Nagel SR. 2002 Crumpling a thin sheet. *Phys. Rev. Lett*. **88**, 076101. (doi:10.1103/PhysRevLett.88.076101)
56. Weaire D, Langlois V, Saadatfar M, Hutzler S. 2007 Foam as granular matter. In *Granular and complex materials* (eds T Aste, T Di Matteo, A Tordesillas), pp. 1–26. Singapore: World Scientific. (doi:10.1142/9789812771995_0001)
57. Firouzi M, Nguyen AV. 2014 Effects of monovalent anions and cations on drainage and lifetime of foam films at different interface approach speeds. *Adv. Powder Technol*. **25**, 1212–1219. (doi:10.1016/j.apt.2014.06.004)
58. Quinn JJ, Sovechles JM, Finch JA, Waters KE. 2014 Critical coalescence concentration of inorganic salt solutions. *Miner. Eng*. **58**, 1–6. (doi:10.1016/j.mineng.2013.12.021)
59. Lambert J, Cantat I, Delannay R, Mokso R, Cloetens P, Glazier JA, Graner F. 2007 Experimental growth law for bubbles in a moderately ‘wet’ 3D liquid foam. *Phys. Rev. Lett*. **99**, 058304. (doi:10.1103/PhysRevLett.99.058304)
60. Wang L, Yoon RH. 2006 Stability of foams and froths in the presence of ionic and non-ionic surfactants. *Miner. Eng*. **19**, 539–547. (doi:10.1016/j.mineng.2005.09.006)
61. Jarek E, Warszynski P, Krzan M. 2016 Influence of different electrolytes on bubble motion in ionic surfactants solutions. *Colloids Surf. A* **505**, 171–178. (doi:10.1016/j.colsurfa.2016.03.071)
62. Czakaj A, Kannan A, Wiśniewska A, Grześ G, Krzan M, Warszyński P, Fuller GG. 2020 Viscoelastic interfaces comprising of cellulose nanocrystals and lauroyl ethyl arginate for enhanced foam stability. *Soft Matter* **16**, 3981–3990. (doi:10.1039/C9SM02392E)
63. Besson S, Debrégeas G, Cohen-Addad S, Höhler R. 2008 Dissipation in a sheared foam: from bubble adhesion to foam rheology. *Phys. Rev. Lett*. **101**, 214504. (doi:10.1103/PhysRevLett.101.214504)
64. Denkov ND, Tcholakova S, Golemanov K, Ananthpadmanabhan KP, Lips A. 2009 The role of surfactant type and bubble surface mobility in foam rheology. *Soft Matter* **5**, 3389–3408. (doi:10.1039/b903586a)
65. Marze S, Guillermic RM, Saint-Jalmes A. 2009 Oscillatory rheology of aqueous foams: surfactant, liquid fraction, experimental protocol and aging effects. *Soft Matter* **5**, 1937–1946. (doi:10.1039/b817543h)
66. Costa S, Höhler R, Cohen-Addad S. 2013 The coupling between foam viscoelasticity and interfacial rheology. *Soft Matter* **9**, 1100–1112. (doi:10.1039/C2SM26644J)
67. Machale J, Akrong DA, Mohammadzadeh O, Telmadarreie A, Yethiraj A, James LA. 2023 Foam-Assisted Enhanced Oil Recovery: Bridging the Gap between Theory and Practice. In *36th International Symposium for the Society of Core Analysts (SCA)*, Abu Dabi, UAE. (doi:10.5281/zenodo.15900319)
68. Jones SA, Getrouw N, Vincent-Bonnieu S. 2018 Foam flow in a model porous medium: I. The effect of foam coarsening. *Soft Matter* **14**, 3490–3496. (doi:10.1039/C7SM01903C)
69. Izawa T, James LA, Yethiraj A. 2026 Supplementary material from: The decay of saline surfactant foams: a study at macroscopic and bubble scales. Figshare. (doi:10.6084/m9.figshare.c.8304092)